Journal of Applied Fluid Mechanics, Vol. 17, No. 7, pp. 1552-1567, 2024.
Available online at www.jafmonline.net, ISSN 1735-3572, EISSN 1735-3645.
https://doi.org/10.47176/jafm.17.7.2361

Efficient Surrogate-based Optimization of the Aerodynamic Performance of a Contra-rotating Open Rotor Utilizing an Infilling Criterion

Q. Wang[1], L. Zhou[1,2†] and Z. Wang[1]

[1] *School of Power and Energy, Northwestern Polytechnical University, Xi'an Shaanxi,710129, China*
[2] *Innovation Center for Advanced Aero-Engine, Beijing,100191, China*

†Corresponding Author Email: zhouli@nwpu.edu.cn

ABSTRACT

This study presents an efficient surrogate-based optimization (SBO) method of the aerodynamic performance of a contra-rotating open rotor (CROR). The objective was to maximize propulsion efficiency while reaching the target thrust coefficient at the cruise condition. To reduce the sample size and improve the optimization convergence speed, an infilling criterion was proposed based on the features of the interaction between the CROR front and rear rotors. The efficient front and rear rotors of the initial samples were selected and then combined to form the infilled samples. The results show that the infilled samples were closer to the Pareto front than the initial samples. For the six optimization parameters, 20 initial sample points were used, 11 samples were infilled, and the surrogate-based optimization was completed in five iterations. In total 43 samples were calculated during the optimization. The number of overall samples is approximately seven times the number of optimization parameters. The optimization results in parameter changes compared to the baseline and improved propulsion efficiency while meeting the thrust target. The optimization process increases the torque share of the rear rotor and changes the flow state at different radial positions, leading to a more uniform total pressure distribution at the outlet position, both circumferentially and radially.

Article History

Received October 7, 2023
Revised December 30, 2023
Accepted February 3, 2024
Available online April 30, 2024

Keywords:

Aerodynamic optimization
Contra-rotating open rotor
Infilling criterion
Propulsion efficiency
Surrogate-based optimization

1. INTRODUCTION

Contra-rotating open rotor (CROR) engines can reduce fuel consumption by up to 25% compared to equivalent turbofan engines (Bellocq et al., 2014; Guérin et al., 2014). This fuel-saving advantage significantly depends on the CROR's propulsion efficiency (Bellocq et al., 2015). To maximize this advantage, the CROR's aerodynamic performance at cruising conditions must be optimized.

High computational costs are incurred during optimization to evaluate each candidate design's performance. Surrogate-based optimization (SBO) reduces the consumption of computational resources by establishing the relationship between the objective function and design parameters through a surrogate model using a limited set of samples, and then searches for the optimal design. The selection of samples for building the surrogate model was completed using the design of experiments (DOE; Giunta et al., 2003). To avoid wasting samples, the projections onto each variable axis of the samples were uniform (Forrester & Keane 2009). Typical techniques include Latin hypercube sampling (LHS; Giunta et al., 2003) and uniform design (UD; Fang et al., 2000).

Various SBO algorithms, in particular efficient global optimization (EGO) and its different versions (Jones et al., 1998; Viana et al., 2013), have been widely applied in the optimization of turbomachinery (Samad et al., 2008; Persico et al., 2019; Baert et al., 2020; Yu et al., 2020; Adjei et al., 2021; Boulkeraa et al., 2022; Tang et al., 2022) and wings (Han et al., 2018). In terms of the SBO of CROR. Schnell et al. (2012) optimized the aerodynamic and acoustic performance of a CROR. Approximately 1600 samples were calculated for 100 free optimization parameters during the optimization process. Villar et al. (2018) developed a platform for designing and optimizing turbomachinery based on evolutionary algorithms. The thrust coefficient and efficiency were used as the objective functions for optimization. The geometry was

NOMENCLATURE

Parameters

A	annular Area
c	chord
$\tilde{c}$	normalized chord
c_z	variation of the chord length
C_T	thrust coefficient predicted by the surrogate model
$C_T = \frac{T}{\rho n^2 D^4}$	thrust coefficient
$C_P = \frac{P}{\rho n^3 D^5}$	power coefficient
$C_p = \frac{p - p_\infty}{\frac{1}{2}\rho_\infty v_\infty^{\ 2}}$	static pressure coefficient
D	diameter of the rotor
e	relative error between the predicted value and the result of CFD calculation
e_η	relative error in propulsion efficiency prediction
e_{C_T}	relative error in thrust coefficient prediction
$f(x)$	propulsion efficiency predicted by surrogate model
$g(x)$	thrust coefficient predicted by the surrogate model
J	advance ratio
n	rotation speed
p	static pressure
P	shaft power
PQA	total power coefficient
Q	torque
R_{tip}	rotor radius
R_{hub}	hub radius
T	thrust
v_s	ship speed
$\mathbf{x}$	optimization parameters matrix

Greek symbols

β	stagger angle
θ	camber angle
$\Delta\theta$	variation of the stagger angle
$\Delta\beta$	variation of the camber angle
ρ	density
$\eta = \frac{C_T}{C_P} J$	propulsion efficiency
η	propulsion efficiency predicted by surrogate model
ξ	displacement in the axial direction
ψ	deviation angle in the tangential direction
λ	penalty function

Subscripts

f	front rotor
r	rear rotor
∞	far field

Abbreviations

CFD	Computational Fluid Dynamics
CROR	Contra-Rotating Open Rotor
CST	Class Shape Transformation
DOE	Design Of Experiments
EI	Expected Improvement
EGO	Efficient Global Optimization
FR	Front Rotor
GA	Genetic Algorithm
LCB	Low Confidence Bound
LE	Leading Edge
LHS	Latin Hypercube Sampling
MP	Minimize Prediction
MSE	Mean Square Error
PI	Probability Improvement
PS	Pressure Surface
RR	Rear Rotor
SBO	Surrogate-Based Optimization
SS	Suction Surface
TE	Trailing Edge
UD	Uniform Design

parameterized employing 44 variables. The optimization process was completed using 1650 computational evaluations. Kwon et al. (2016) performed SBO for four design parameters: the radii of the front and rear rotors, pitch angle of the rear rotor, and rotor spacing. Using the LHS technique, 77 sample points in total were obtained. Villar et al. (2019) performed two independent aerodynamic optimizations of the CROR with different blade profiles, including a class shape transformation (CST) profile with 108 design parameters and NACA16 with 44 design parameters. Due to the constraint of utilizing an equivalent quantity of computational resources, the CST optimization process is non-converged and has unexploited potential for improvement. In this particular case, the NACA 16 optimization performed better than the CST. The aerodynamic optimization of the CROR could be accomplished using the SBO. However, the number of samples required for optimization was at least 16 times the number of design parameters. This poses a challenge to computational resources and the final optimization results.

In order to minimize the quantity of samples needed to solve the optimization problem while ensuring the accuracy of the Pareto front, infilling criteria were used to sample the objective function in promising areas during the optimization process (Forrester & Keane 2009). Infilling criteria were proposed based on the mathematical process of surrogate models, such as minimize prediction (MP; Booker et al.,1999), or on the information provided by the surrogate model, such as the expected improvement (EI), probability improvement (PI; Jones 2001), mean square error (MSE; Sasena et al., 2002) and low confidence bound (LCB; Jones, 2001) for surrogate optimization algorithms based on the Kriging model. However, there was a direct correlation between the surrogate model's accuracy and the locations of the infilled samples. The infilled point may be useless if the surrogate model deviates from the real model (Liu et al., 2022), thereby weakening the effect of the infilling criteria in reducing the overall sample size.

To solve this challenge, in this study, an infilling criterion is proposed based on the features of the rotor interaction, and detailed implementation steps are provided. Subsequently, surrogate-based optimization of the aerodynamic performance of a CROR was performed by utilizing this infilling criterion. Infilled samples were obtained before constructing the surrogate model To prevent the impact of the surrogate model's accuracy. The number of samples used during the optimization was approximately seven times the number of optimization parameters. The remainder of this paper is organized as follows. First, details of the baseline design of the CROR are presented. The parameterization approach of the CROR is described. The numerical methodology and validation of computational fluid dynamics (CFD) are presented. Subsequently, features of rotor interaction are analyzed and an infilling criterion is posed. An SBO algorithm with this infilling criterion is subsequently presented. Finally, the validation of the infilling criterion and optimization results are discussed in detail, and conclusions are provided.

2. BASELINE CONFIGURATION

The baseline CROR has a flight height of 10,668 m and a design cruise Mach number of 0.785. It has 12 blades in the front rotor (FR) and rear rotor (RR), each with a diameter of 4 m and a hub ratio of 0.4. The rotor was rotated at 1000 rpm, and the distance between the FR and RR was 0.9 m. The circular velocity of the blade tip was 209 m/s. The baseline geometry is shown in Fig. 1.

The profiles at various radial positions were stacked to form the three-dimensional geometry of the CROR. The stacking line connected the centers of gravity of each profile. It includes an axial sweep and tangential leaning at different radial positions. The definitions of sweep and lean are shown in Fig. 2. The axial sweep ξ can be defined as the displacement in the axial direction. The tangential leaning is defined as the deviation angle ψ in the tangential direction.

The stacking line, which was used as the baseline, is shown in Fig. 3. The rotors have a significant aft-sweep in the top and middle positions, which is intended to reduce the shock wave drag owing to the high flight Mach numbers. Both rotors were shaped to lean toward the side of the pressure surface.

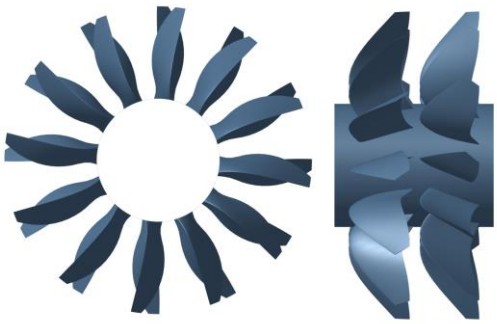

Fig. 1 Geometry of CROR baseline

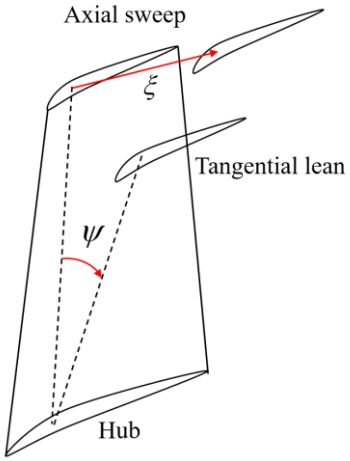

Fig. 2 Stacking line definition

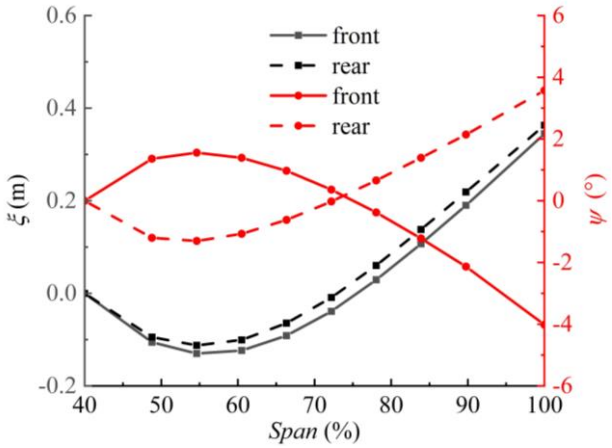

Fig. 3 Radial distribution of stacking line parameters

Two-dimensional cross-section of the CROR included the mean camber line and thickness profile. NACA0016 was used to obtain the thickness profile. The mean camber line was a double-circular arc. The parameters of the two-dimensional cross-sectional airfoil

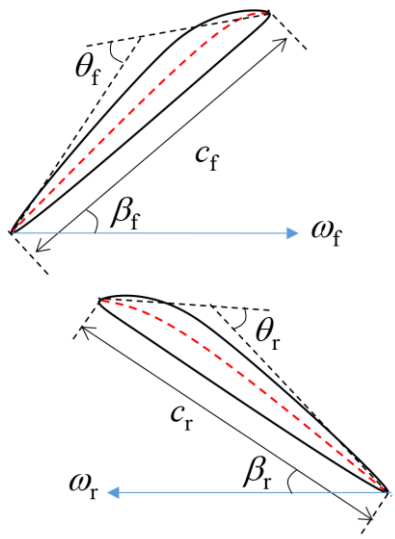

Fig. 4 Parameterization of blade profiles

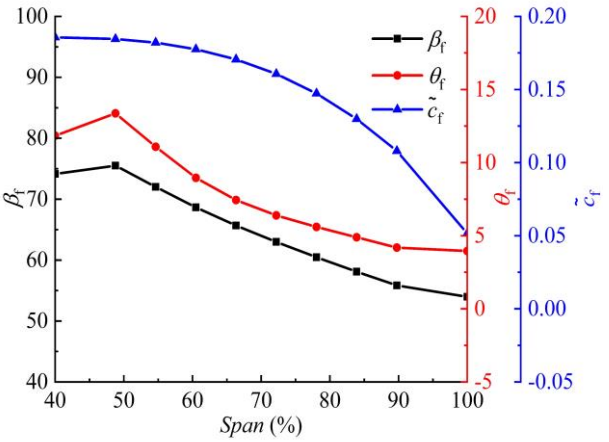

(a) Profile parameters of FR

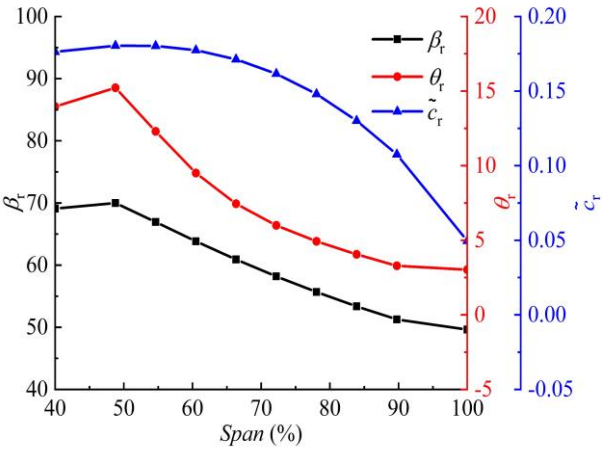

(b) Profile parameters of RR

Fig. 5 Profile parameters along the radial direction

included the camber angle, stagger angle, and chord length, as shown in Fig.4. The stagger angle was defined as the angle between the chord and the rotational direction.

Two-dimensional section parameters of the baseline are shown in Fig.5. The chords were normalized to the diameter.

$$\tilde{c} = c / D \tag{1}$$

3. NUMERICAL SIMULATION METHOD

3.1 Evaluation of Aerodynamic Performance of CROR

The aerodynamic performance of the CROR was evaluated based on the overall propulsion efficiency and thrust coefficient. The blade surface pressure and viscous forces were the main elements used in the CROR thrust computation. The pressure and viscous forces on the blade surface can be obtained from the surface integral of the pressure and viscous shear force. The combined force in the axial direction was the thrust of the blades. The overall thrust was calculated as the sum of both the front and rear rotors' thrust. The shaft power of the rotor is the product of the angular velocity and the torque of the blades. The thrust and power coefficients of the overall CROR are defined as follows.

$$C_T = \frac{T}{\rho n^2 D^4} \tag{2}$$

$$C_P = \frac{P}{\rho n^3 D^5} \tag{3}$$

The thrust and power coefficients of the front and rear rotors were calculated using their thrust and power. The advance ratio of the CROR is defined as:

$$J = \frac{v_s}{nD} \tag{4}$$

The CROR's overall propulsion efficiency is defined as:

$$\eta = \frac{C_T}{C_P} J \tag{5}$$

The propulsion efficiency of each rotor was calculated using the same formula and their thrust and shaft power.

3.2 Numerical Simulation

The flow field was solved by steady calculation using the commercial software FINE TURBO. A central difference scheme was used for spatial discretization. The ideal gas was selected as the working fluid and the Spalart-Allmaras model was used as the turbulence model. The grid used for the calculations was generated using AUTOGRID5, and its topology included standard O-type grids surrounding the blade and H-type grids inside the blade channel. The length of the first layer grid was 1×10^{-5} m. The y-plus value was under 10 thus meeting the requirements of the turbulence model. Figure 6 shows the grid.

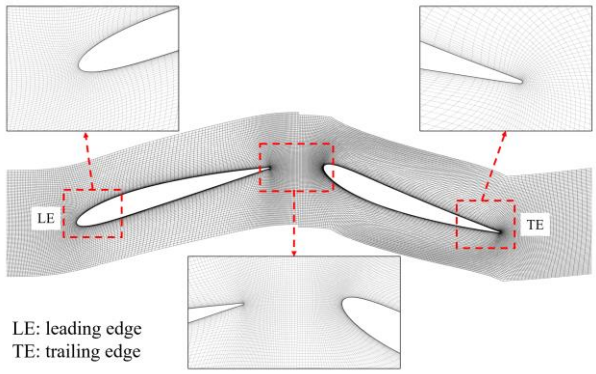

Fig. 6 Computational grid

The calculation was done using a single-blade channel. When selecting the computation region for the calculation of a CROR, the effect of far-field radius was taken into consideration. To eliminate the impact of the limited region size on the calculation of the rotors, it must reach sufficiently far into the far field. The disturbance range of the CROR to the surroundings was considered (Zachariadis & Hall 2011; Sohoni et al., 2019). For a far-field of 3.62 tip radius, further expanding the radial size of the domain did not produce any enhancements (Zachariadis & Hall 2011). In this study, the far front boundary distance from the front propeller disk was eight times the radius, the far rear boundary distance from the rear propeller disk was eight times the radius, and the radial far-field boundary radius was six times the radius. Consequently, the contra-rotating open rotor did not affect the flow throughout the entire radial far-field boundary. Therefore, for radial far-field boundaries, far-field or pressure inlet boundaries no longer affect the calculation results (Numeca International, 2009). Figure 7 shows the detailed boundary condition. The inlet boundary was given the total pressure, total temperature, and velocity direction. The outlet boundary was given the static pressure. The blade and hub surfaces are adiabatic walls. The interface adopts a mixing plane condition, which is commonly used in numerical simulations of CRORs (Zachariadis & Hall 2011; Jaron et al., 2018).

The numerical simulation method adopted in this study was validated using the F7A7 scale model. This

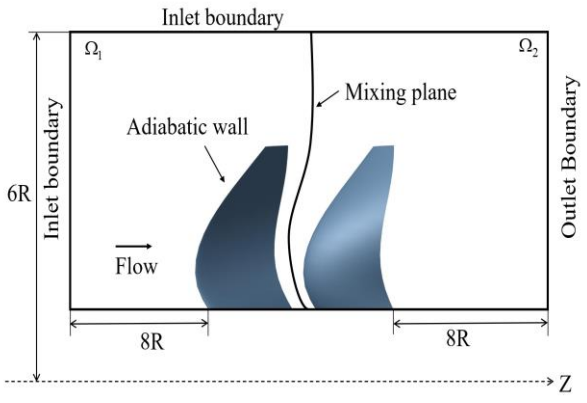

Fig. 7 Boundary condition of numerical simulation

model has a design Mach number of 0.72. The design advance ratio is 2.82. The blades were tested using model propulsion simulators (MPS) which consisted of blades, a hub, a center shaft, a nacelle, etc (GE36 Design and Systems Engineering, 1987; Hoff et al., 1990). The total power coefficient of the CROR is defined as follows:

$$PQA = \frac{P}{A\rho n^3 D^3} \tag{6}$$

where A is the flow area, defined as:

$$A = \pi\left(R_{tip}{}^2 - R_{hub}{}^2\right) \tag{7}$$

with R_{tip} and R_{hub} being the radii of the rotor and the hub.

A comparison between the CFD and experimental results is shown in Fig.8. The advance ratio can be changed by varying the rotational speed (Hoff, et al., 1990). The distribution of the *PQA* under different advance ratios is shown in Fig.8 (a). There was good agreement between the numerical simulation and experimental results. At the design advance ratio, the relative error of the total power coefficient between the CFD simulation and the experiment was less than 1%. The results only differed when CROR significantly deviated from the design points. In Fig. 8(b), the trend in the efficiency obtained by CFD remains consistent with the experimental values, and the highest efficiency values correspond to the experimental data. As shown in Fig. 8(c), the trends of the CFD and experimentally obtained torque ratios are similar when the advance ratio is varied. Numerical simulation methods can be used to obtain the changes in the overall performance of the front and rear rotors owing to the interaction between the rotors. The experimentally obtained torque ratio decreased more rapidly than the CFD results. At the working point which is far from the design point, there is a difference between the overall performances obtained by CFD and the experiment, possibly because of the different levels of deformation of the blade under different advance ratios. This difference was also observed in the comparison between the CFD and experimental results (Zachariadis & Hall 2011). All the aforementioned evaluations have conclusively shown that the numerical method used in this study has sufficient accuracy and completely satisfies the calculation requirements. The interaction between two rows of rotors was reflected in the change in performance of the CRORs using this numerical simulation method.

The grid convergence index (*GCI*) (Roache, 1997) was employed to verify the grid independence. When calculating the *GCI*, the safety factor was 3. The thrust and power coefficients of the CROR were chosen as the key variables. The final calculated *GCI* values under three grids are listed in Table 1. Coarse, medium, and fine grids are indicated by the subscripts 1, 2, and 3, respectively. N is the quantity of grid cells. f denotes the calculated key variables. ε_{12} denotes the absolute error between the results obtained by medium and coarse grids. ε^{12} indicate the relative errors between the results calculated by

Table 1 GCI for grid independence study

Parameters	C_T	C_P
N_1, N_2, N_3	1662278, 3911810, 8448730	1662278, 3911810, 8448730
f_1, f_2, f_3	0.936, 0.869, 0.865	3.457, 3.209, 3.195
$\varepsilon_{12}, \varepsilon_{23}$	-0.067, -0.004	-0.248, -0.014
$\varepsilon^{12}, \varepsilon^{23}$	0.077, 0.005	0.077,0.004
GCI_{12}, GCI_{23}	0.0177, 0.0013	0.0130, 0.0007

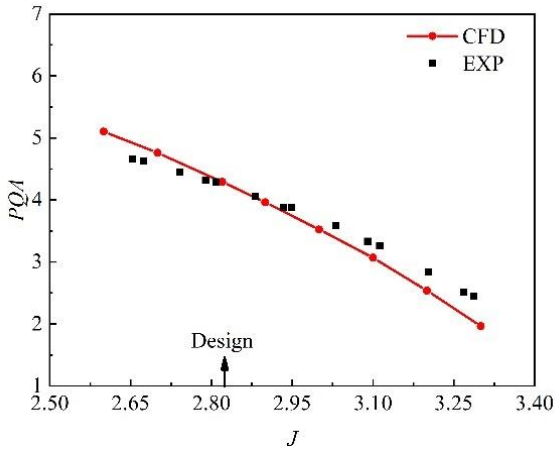

(a) Comparison of *PQA* under different advance ratios

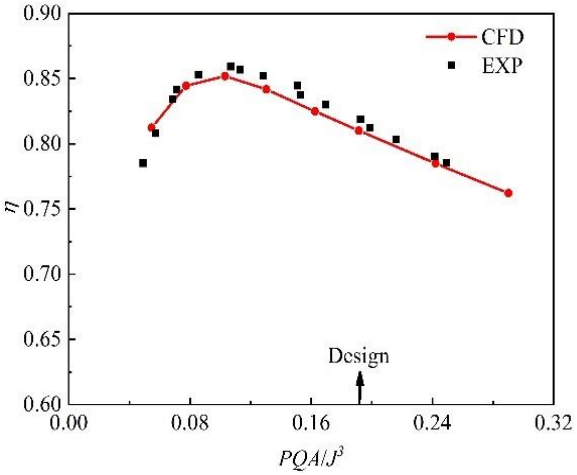

(b) Comparison of the propulsion efficiency under different advance ratios

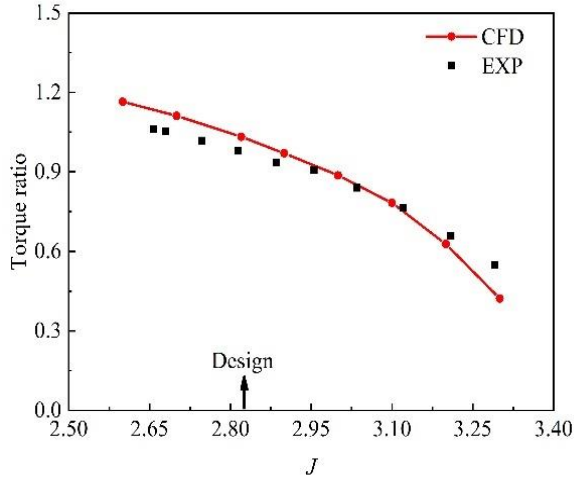

(c) Comparison of the torque ratio under different advance ratios

Fig. 8 Comparison of CFD and experiment results

medium and coarse grids. GCI_{12} denotes the computed grid convergence index between the coarse and medium grids.

The ε^{23} for the power coefficient was 0.4% and the ε^{23} for the thrust coefficient was 0.5%. Meanwhile, compared with the calculated GCI for medium and coarse grids, those for fine and medium grids were lower. A medium grid with approximately 4 million cells was selected in this study after considering the results of the GCI calculations of the three sets of grids.

4. SBO WITH INFILLING CRITERION

4.1 Mathematical Description of the Optimization Problem

Optimizing the aerodynamic performance of CRORs is necessary during the early stages of the aerodynamic design process. As the main thrust-generating component is a contra-rotating open rotor under cruise conditions, a high propulsion efficiency must be achieved while reaching the target thrust coefficient. The chord lengths, camber angles, and stagger angles of the front and rear rotors were selected as the optimization parameters. Thus, the problem of aerodynamic optimization of the CROR can be formulated as

$$\begin{cases} \mathbf{x} = \left[\theta_{\mathrm{f}}, \beta_{\mathrm{f}}, c_{\mathrm{f}}, \theta_{\mathrm{r}}, \beta_{\mathrm{r}}, c_{\mathrm{r}}\right] \\ \mathbf{x} \in \left(\mathbf{x}_{\min}, \mathbf{x}_{\max}\right) \\ \eta = f\left(\mathbf{x}\right) \\ C_T = g\left(\mathbf{x}\right) \\ \max\left(\eta\right) \\ C_T \in \left(C_{T,\mathrm{lower}}, C_{T,\mathrm{upper}}\right) \end{cases} \tag{8}$$

During the optimization process, the chord lengths, camber angles, and stagger angles of the front and rear rotors were changed to produce a new geometry. The geometric parameters of the new samples differ from those of the baseline in the following ways:

$$\begin{cases} \theta_{\mathrm{f}} = \theta_{\mathrm{f,baseline}} + \Delta\theta_{\mathrm{f}} \\ \beta_{\mathrm{f}} = \beta_{\mathrm{f,baseline}} + \Delta\beta_{\mathrm{f}} \\ c_{\mathrm{f}} = c_{\mathrm{f,baseline}} \cdot c_{\mathrm{z,f}} \\ \theta_{\mathrm{r}} = \theta_{\mathrm{r,baseline}} + \Delta\theta_{\mathrm{r}} \\ \beta_{\mathrm{r}} = \beta_{\mathrm{r,baseline}} + \Delta\beta_{\mathrm{r}} \\ c_{\mathrm{r}} = c_{\mathrm{r,baseline}} \cdot c_{\mathrm{z,r}} \end{cases} \tag{9}$$

Table2 Range of optimization parameters

Parameter	Minimum	Maximum
$\Delta\theta_f$	-2°	2°
$\Delta\beta_f$	-2°	2°
$c_{z,f}$	0.8	1.2
$\Delta\theta_r$	-2°	2°
$\Delta\beta_r$	-2°	2°
$c_{z,r}$	0.8	1.2

$\Delta\theta$, $\Delta\beta$, and c_z represent the variations in the stagger angle, camber angle, and chord length, respectively. The range of the optimization parameters was determined from the results of previous parametric studies (Hoff, et al., 1990; Li, et al., 2022). The design space was sufficiently large to ensure that an optimal point could be obtained. The ranges of the optimization parameters are shown in Table2.

4.2 Infilling Criterion Based On Features

The thrust coefficient and propulsion efficiency are incongruent with the optimization of the aerodynamic performance of a CROR. A possible Pareto front is shown in Fig.9. The final optimization objective is to determine a section of the Pareto front that satisfies the target thrust coefficient. Consequently, when building a surrogate model for the optimization, the value of the Pareto front close to the optimization target should be considered as more than the overall accuracy of the surrogate model. However, the initial samples obtained for constructing the surrogate model were typically located at a certain distance from the Pareto front. To complete the optimization process, the infilling criterion must cause the infilled samples to move toward the Pareto front. Furthermore, the characteristics of the constructed surrogate model are related to the interaction features between the front and rear rotors. Based on this hypothesis, the features of interaction are analyzed, and the infilling criterion used in this study is proposed based on research on the interaction between rotors of the CROR.

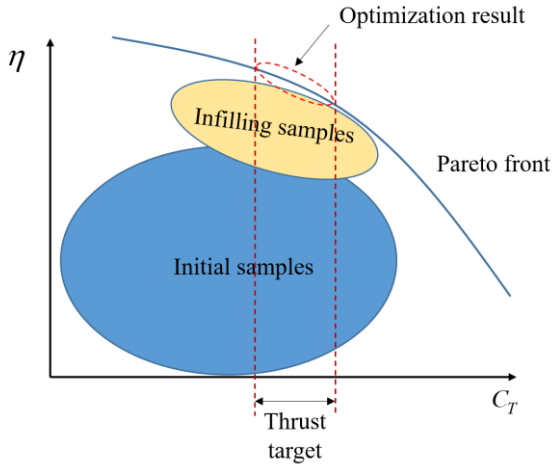

Fig. 9 Schematic diagram of the optimization problem

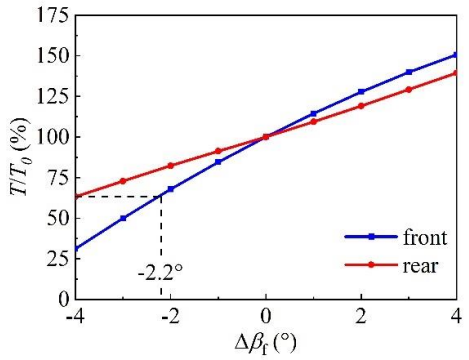

(a) Thrust

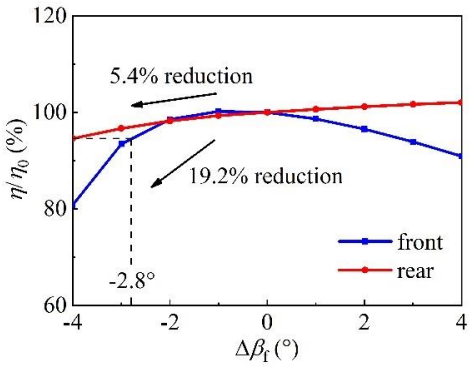

(b) Propulsion efficiency

Fig. 10 The performance of rotors with different front stagger angles

4.2.1 Features of Rotors' Interaction

In the CROR, the rotors exhibit complicated interactions with each other (Dubosc et al., 2014; Slaboch et al., 2017). The presence of induced velocity causes interactions between the rotors. Additionally, because of the wake flow of the FR, the RR is greatly affected by the FR. By altering the state of the FR outlet, the RR will also have an impact on the flow state of the FR. In this study, stagger angles of the front and rear rotors were changed to analyze the features of the rotor interaction. The analysis was on the influence of the features on the variation in the propulsion efficiency and thrust.

Figure 10 shows the effect of the front stagger angle on the thrust and propulsion efficiency of the rotors. As the front rotor stagger angle increased, the thrust increased rapidly for both rows of rotors, and the propulsion efficiency increased and then decreased for the FR and increased slowly for the RR.

During a change in the front rotor stagger angle, there are fewer changes in the rear rotor's performance. When the front rotor stagger angle was reduced by 4 degrees, the change in thrust at the RR was as large as that at the FR when the front rotor stagger angle was reduced by 2.2 degrees. In terms of propulsion efficiency, when the front rotor stagger angle was reduced by 4 degrees, the change in the efficiency of the RR was only equal to the change in the efficiency of the FR when the front rotor stagger angle was reduced by approximately 2.8 degrees. When the stagger angle of the FR was reduced by 4 degrees, the efficiency of the FR decreased by 19.2%, whereas the efficiency of the RR decreased by only 5.4%.

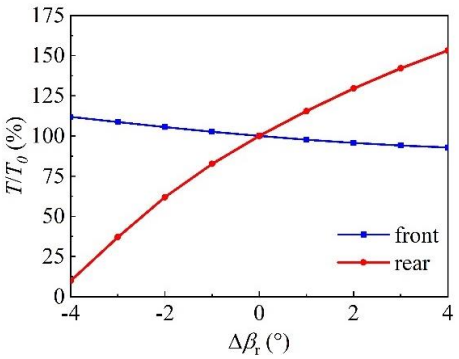

(a) Thrust

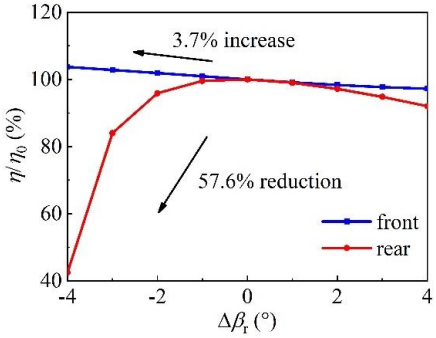

(b) Propulsion efficiency

Fig. 11 The performance of rotors with different rear stagger angles

This feature was related to the effect of the FR on the RR. A change in the front stagger angle causes a change in the angle of incidence of the FR. The angle of incidence increases as the stagger angle increases; therefore, the front rotor thrust increases. Consequently, as the stagger angle of the FR increases, the relative flow angle at the front rotor outlet increases, thus increasing the rear rotor's angle of incidence, and thrust.

However, based on the velocity triangle, the change in the angle of incidence of the RR was smaller than that of the FR. Furthermore, as the front airflow turning angle increased, the deviation angle also increased (Cetin et al., 1987), making the variation in the relative flow angle at the front outlet less than ideal. These two factors are combined to limit the effect of the FR on the RR, which is reflected in the fact that the FR has less influence on the RR as it moves away from the optimum operating conditions.

Figure 11 shows a comparison of the performances of the rotors with different rear stagger angles. As the rear rotor stagger angle increased, the rear rotor's thrust increased rapidly, whereas that of the FR decreased slightly. The rear rotor's propulsion efficiency increases and then decreases. However, the front rotor's propulsion efficiency remains approximately constant.

When the rear rotor stagger angle increased, the angle of incidence of the RR increased This results in an immediate and noticeable change in the rear rotor's thrust and propulsion efficiency. However, no significant effect was exerted on the front rotor's flow conditions because the effect of the RR was achieved by changing the outlet pressure of the FR. This has a limited impact on the performance of the FR. For the propulsion efficiency, a reduction in the rear rotor stagger angle by 4 degrees only increases the front rotor efficiency by 3.7%, whereas the rear rotor efficiency decreases by 57.6%.

In conclusion, the above analysis shows that in a CROR, the thrust of rotors interacts. A change in the parameters of the FR, that results in a change in the thrust of the FR, must be accompanied by a change in the thrust of the RR as well. The overall thrust was affected by the combination of the two rows of rotors. However, the interaction between the rotors had less impact on the propulsion efficiency. The propulsion efficiency of the rotors depends on their parameters. For example, when the flow state of the FR significantly deteriorates, resulting in a significant reduction in propulsion efficiency, the rear rotor efficiency is not significantly reduced. When the RR deteriorates significantly, the flow state of the FR is not affected very much either. In addition, this phenomenon is more apparent if the rotor is efficient because there is a flat area near the maximum efficiency point.

Furthermore, the magnitude of change in thrust exceeds that of the propulsion efficiency when parameters change. If an efficient configuration is obtained, a wide range of thrust adjustments can be made by adjusting the geometric parameters without significantly reducing the propulsion efficiency. This implies that the propulsion efficiency is more important than the thrust in the optimization problem.

4.2.2 Infilling Criterion

According to the above analysis, the performance of the rotors depends more on their parameters. Thus, the FR of a CROR remains efficient when paired with another rear rotor within a certain range. The RR also exhibits this characteristic. Thus, by selecting efficient front and rear rotors from the initial samples and combining them, the new CROR will have both an efficient FR and an efficient RR. The propulsion efficiency of the new CROR will be higher than that of the initial samples, which will bring the infilled samples closer to the Pareto front than the initial samples. This increases the risk of obtaining new samples with too much or too little thrust. Because the optimization objective includes the target thrust, the features of thrust variation are also important. As discussed in section 4.2.1 the thrust can be varied over a wide range while maintaining an almost constant propulsion efficiency. Meanwhile, the presence of initial samples provides direction for adjustment. This makes it possible to implement this method for infilling samples.

4.3 SBO Algorithm with the Infilling Criterion

The detailed flow chart in Fig.12 illustrates the SBO algorithm using the infilling criterion. The flowchart of the standard EGO algorithm is shown on the right side of the flowchart. This includes the parameterization of the CROR, the process of choosing the initial samples by DOE, the construction of the Kriging model, and convergence. The left side shows the infilling criteria used in this study. After the CFD evaluation was completed for the initial sample points, the front and rear rotors with good performance were selected, arranged, and combined to form new samples. This part of the sample was added to the initial sample points and a new surrogate model was built.

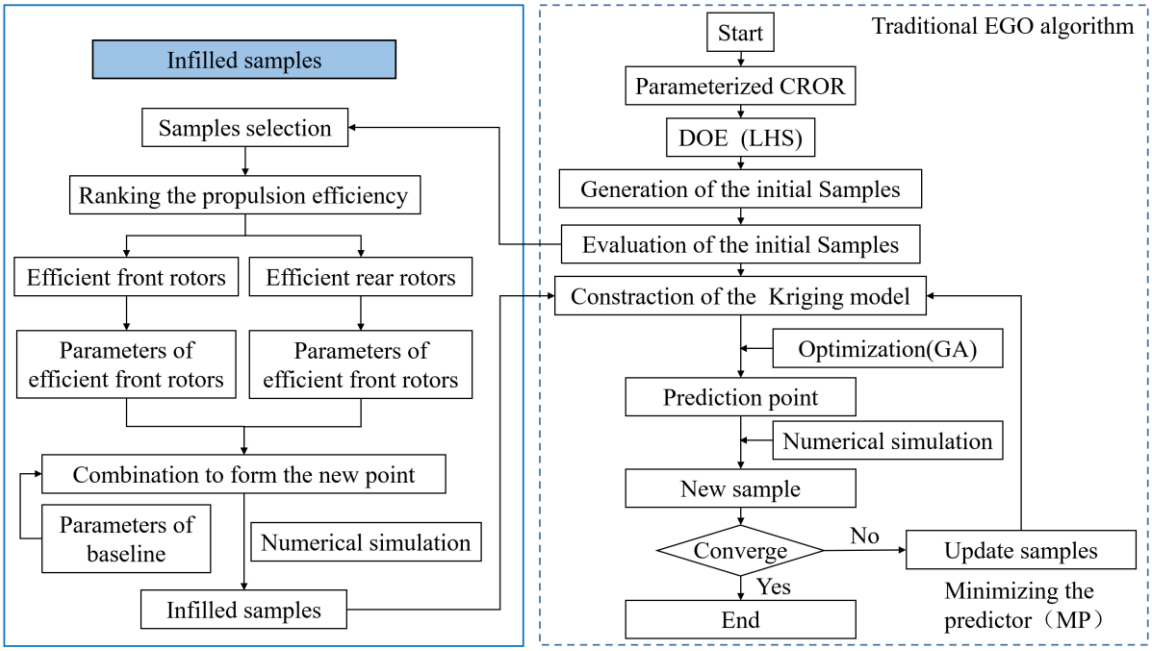

Fig. 12 Flow chart of surrogate-based optimization of CROR with infilling criterion

The MP criterion was applied during the convergence process; if the new sample points did not satisfy the convergence condition, the process was iterated until the convergence condition was attained.

The Kriging model was used in the surrogate model-building process. Models for propulsion efficiency and thrust coefficient were built. The upper and lower bounds of the target coefficient were considered separately as optimization objectives. Thus, multi-objective optimization is transformed into single-objective optimization with constraints. The optimization was solved by a penalty function. The penalty function is expressed as follows:

$$F(x) = \tilde{f}(x) + \lambda \cdot \left[\tilde{g}(x) - C_{T,\text{target}}\right] \tag{10}$$

$\tilde{f}(x)$ and $\tilde{g}(x)$ are the propulsion efficiency and thrust coefficient predicted by the Kriging surrogate model, respectively. The penalty function λ was set to 10000. The upper and lower thrust coefficients of the thrust target in the search for the optimum were 0.962 and 1.036, respectively. During the optimization search process, a genetic algorithm was used.

Convergence is determined by comparing the relative error achieved between the predicted value and the CFD results, with the relative error defined as:

$$e = e_\eta + e_{C_T} \tag{11}$$

where e_η is the relative error in the propulsion efficiency prediction, and e_T is the relative error in the thrust coefficient prediction, which are both defined separately as：

$$e_\eta = \frac{|\eta - \tilde{\eta}|}{\eta} \tag{12}$$

$$e_{C_T} = \frac{|C_T - \tilde{C}_T|}{C_T} \tag{13}$$

where C_T and η are the calculated thrust coefficient and propulsion efficiency values, respectively; $\tilde{C}_T$ and $\tilde{\eta}$ are the thrust coefficient and propulsion efficiency predicted using the surrogate model, respectively. When the relative error satisfies the: $e \le 0.5\%$, the upper and lower bounds of the optimization result have converged.

Subsequently, additional validation points are added to the lower and upper bound intervals to verify that the optimization results meet the requirements. When the validation points satisfy $e \le 0.5\%$, the optimization process is regarded as converged and a Pareto front is obtained.

5. RESULTS

For the six optimization parameters shown above, the LHS technique was adopted for the DOE. After the CFD evaluations, 20 initial samples were obtained. The average of the initial samples is denoted as Ref. Ref is not a real sample obtained using CFD but the arithmetic mean of the performance of the initial samples, which denotes the level of initial design space and provides a reference for filtering the points that need to be infilled. According to the infilling criterion, efficient rotors must be selected by ranking the propulsion efficiency, as shown in Fig. 13. R2 represents the rear rotor of the second initial sample, and F3 represents the front rotor of the third initial sample.

The selected efficient front and rear rotors were then combined to yield nine new samples. These samples could potentially gain propulsion efficiency at the expense of the thrust coefficient. To ensure that the thrust coefficients of the infilled points were not too small, the FR and RR of the baseline were selected to be combined with the best

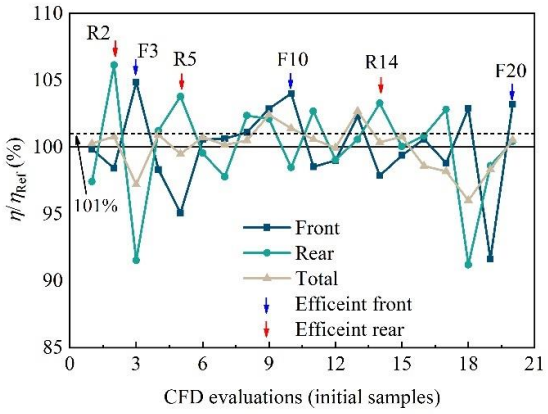

Fig. 13 Samples selection process

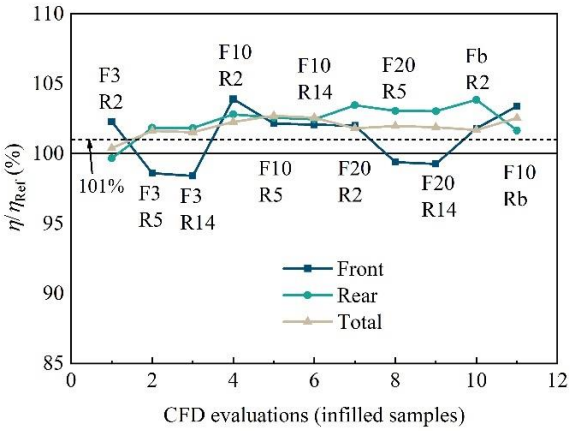

Fig.14 The CFD evaluations of infilling samples

front and rear rotors. Therefore, a total of eleven infilled samples were obtained. CFD evaluations of the 11 infilled samples were performed, as shown in Fig.14. F3R2 represents the infilled sample with the front rotor of the third initial sample and the rear rotor of the second sample. The overall propulsion efficiency of most of the infilled samples improved compared with that of the initial samples. In terms of the overall relative propulsion efficiency, ten of the 11 infilled samples exceeded 101%; however, only two of the 20 initial samples exceeded this threshold. It can also be observed that an efficient rotor remains efficient when paired with another rotor, thus validating the infilling criterion.

Using the initial 20 samples and 11 infilled samples, a surrogate model was built and solved iteratively until convergence. Convergence is achieved after five iterations. Figure 15 shows the iteration results for five iterations. In the fifth round, three additional validation points were calculated provided that the upper and lower thrust coefficients of the thrust target were accurately predicted. The results proved that the optimization in the fifth round satisfies the convergence requirements.

Figure 16 gives the distribution characteristics of the propulsion efficiency and thrust coefficient for the samples, including the baseline, initial samples, average of the initial samples, MP samples, and optimization results. The optimization result with a thrust coefficient of 1.040 is defined as *Opt_a*.

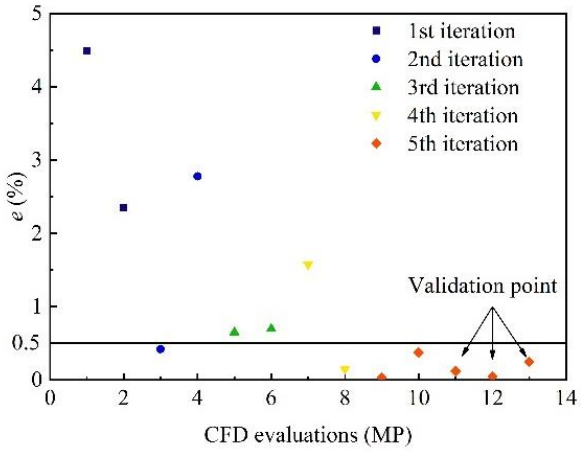

Fig. 15. Convergence history of optimization

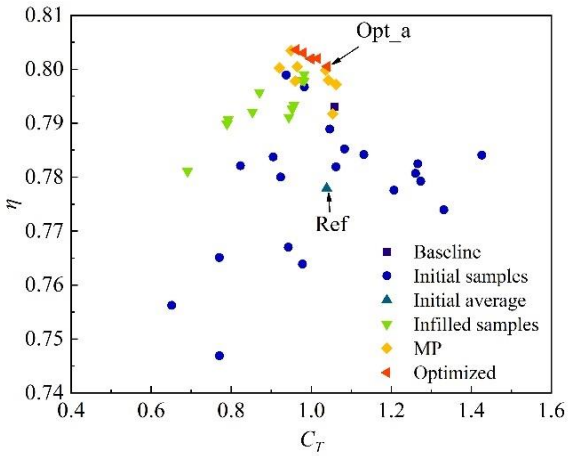

Fig. 16 Optimization trade-off chart

In Fig 16, the baseline is on the upper edge of the entire initial design space, indicating that the baseline is already an efficient geometry and that the SBO further improves the efficiency of the baseline. After applying the infilling criterion, the infilled samples were observed to be more efficient than the initial points. Therefore, the full design space can be extended toward the the Pareto front, thereby achieving the purpose of the infilling points.

A comparison of the CROR performance after SBO is presented in Table 3. The propulsion efficiency of the baseline is 1.94% higher than that in Ref. *Opt_a* was 2.90% more effective than Ref. The torque ratio of *Opt_a* was 20.72% higher than that of the baseline. The gain in the front rotor propulsion efficiency is mostly responsible for *Opt_a* 's increase in propulsion efficiency.

The optimization parameters of *Opt_a* are listed in Table 4. The optimization led to slight reductions in the front camber angle, a reduction in the front stagger angle, and a significant reduction in the chord length. The rear

Table3 Comparison of performance after SBO

	C_T	η	η_f	η_r	Q_r/Q_f
Ref	1.039	0.778	-	-	-
Baseline	1.058	0.793	0.716	0.866	1.045
Opt_a	1.040	0.801	0.731	0.856	1.262

Table 4 Optimization parameters of *Opt_a*

rotor	front		
parameter	$\Delta\theta_f$ (°)	$\Delta\beta_f$ (°)	$c_{z,f}$
Opt_a	-0.07	-0.76	0.81
rotor	rear		
parameter	$\Delta\theta_r$ (°)	$\Delta\beta_r$ (°)	$c_{z,r}$
Opt_a	-1.33	1.98	0.98

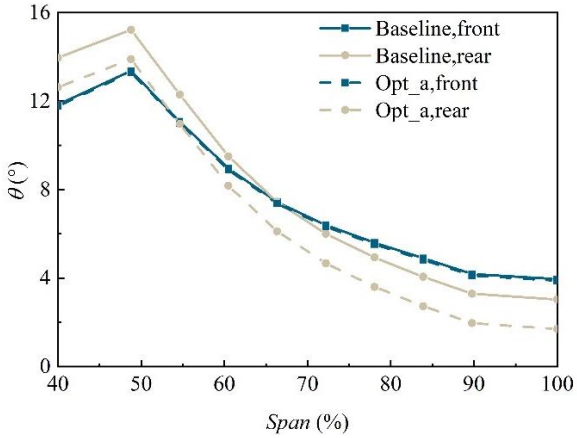

Fig. 17 Comparison of the radial distribution of camber angles

rotor profiles exhibited a reduced camber angle and increased stagger angle, whereas the chord length remained almost unchanged.

A comparison of the radial distributions of the camber angles before and after optimization is shown in Fig.17. It illustrates that the front camber angle is almost unchanged, whereas the camber angle of the RR is significantly reduced.

A comparison of the cross sections at different radial positions for the baseline and optimized CROR is presented in Fig.18 and Fig.19. The results indicate a decrease in the front chord length and an increase in the rear stagger angle.

The radial distribution of the relative flow angles at the inlet and outlet positions is shown in Fig.20. The relative flow angle was the angle between the relative and circumferential velocities. It can be found that the variation in relative flow angle corresponds to the modification of geometry parameters. For the FR, the relative flow angle at the inlet position was almost constant, but the outlet relative flow angle decreased correspondingly because of the reduction in both the blade camber angle and the stagger angle. For the RR, the inlet relative flow angle also decreased, but the outlet relative flow angle was larger because the stagger angle increased more than the blade camber angle.

To illustrate the change in the flow state of the different blade segments before and after optimization, and to further show how this change affects the overall performance of the CROR. The rotors were divided into 10 segments along the radial direction. The blade segment propulsion efficiency is defined as follows:

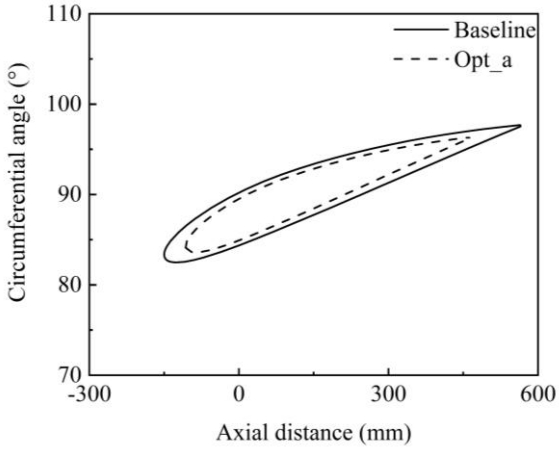

(a) Root of the blade

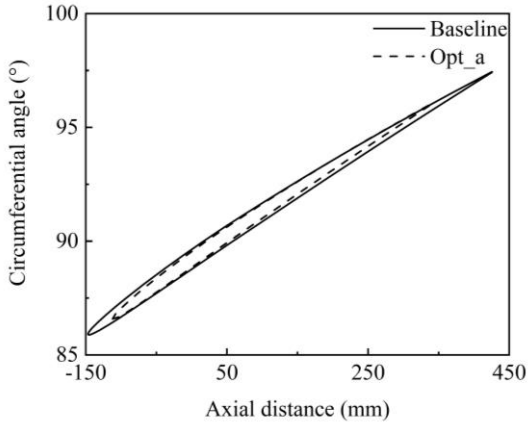

(b) Middle of the blade

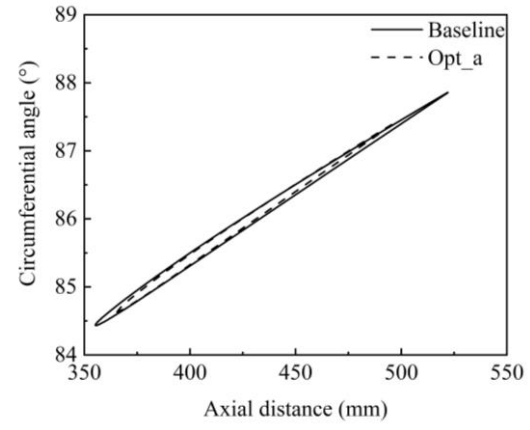

(c) Top of the blade

Fig. 18 Geometry comparison for the FR at different radial positions

$$\eta_i = \frac{T_i \cdot v_S}{Q_i \cdot \omega} \tag{14}$$

where T_i is the thrust of the segment, and Q_i is the torque of the segment. Because the ship speed was used to calculate the overall propulsion efficiency, it was also used in the segment calculation. Thus, the overall propulsion efficiency of the CROR can be expressed as:

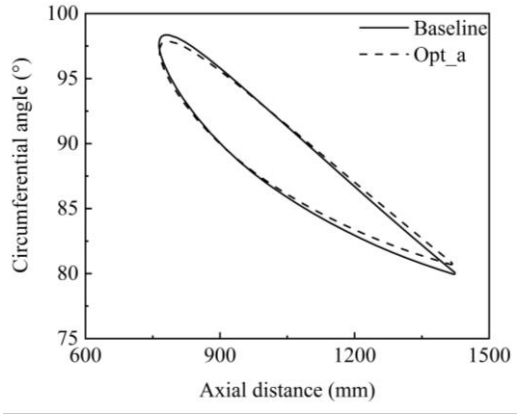

(a) Root of the blade

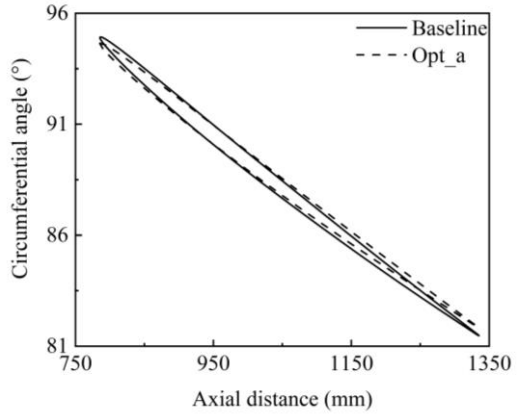

(b) Middle of the blade

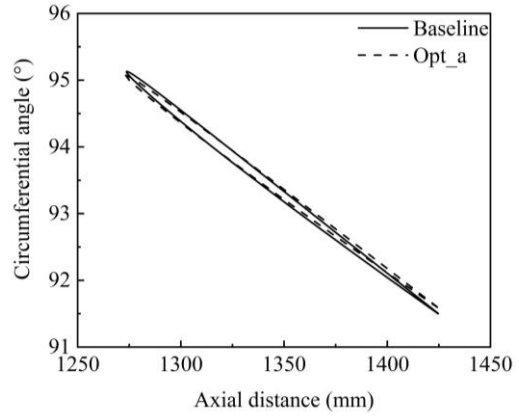

(c) Top of the blade

Fig. 19 Geometry comparison for the RR at different radial positions

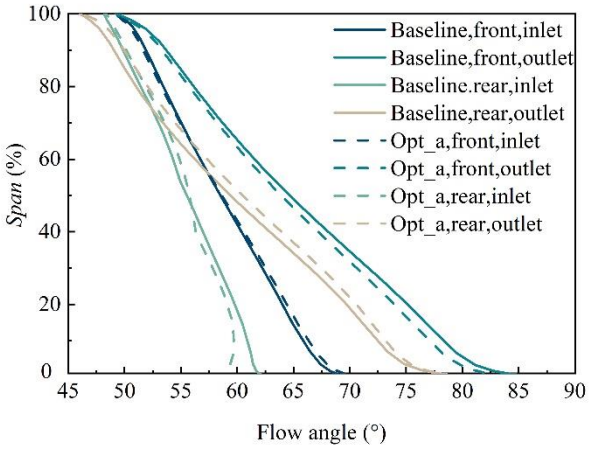

Fig. 20 Comparison of the radial distribution of flow angles

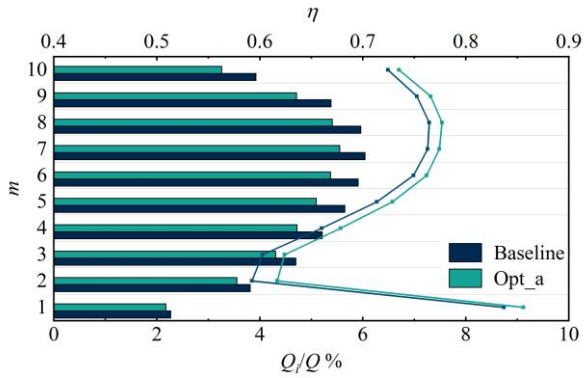

(a) Segments of the FR

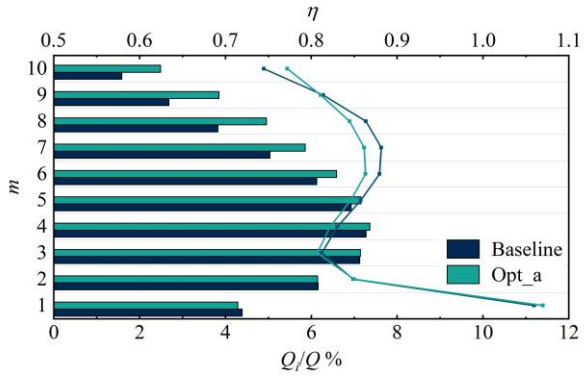

(b) Segments of the RR

Fig. 21 Comparison of propulsion efficiency and torque percentage for each segment

$$\eta = \sum_{i=1}^{20} \frac{Q_i}{Q} * \eta_i \tag{15}$$

Figure 21 shows the results of the comparison between the baseline and *Opt_a*. There was a sudden shift in the propulsion efficiency curve at the root of the blade. This is because the calculated propulsion efficiency exceeded the actual propulsion efficiency because the flow at the root was influenced by the hub layer and the actual axial velocity of the flow at the root was less than the ship speed.

For the FR, the propulsion efficiency of *Opt_a* increased in all radial positions of the segments compared with the baseline, whereas the percentage of torque was significantly lower in all radial positions. This indicates that the power distribution ratio of the FR has decreased. For the RR, the torque percentage increased significantly in the middle and upper positions. At the middle position, an increase in torque led to a slight decrease in the propulsion efficiency; however, the propulsion efficiency at this position exceeded 0.85. At the top of the blade, the

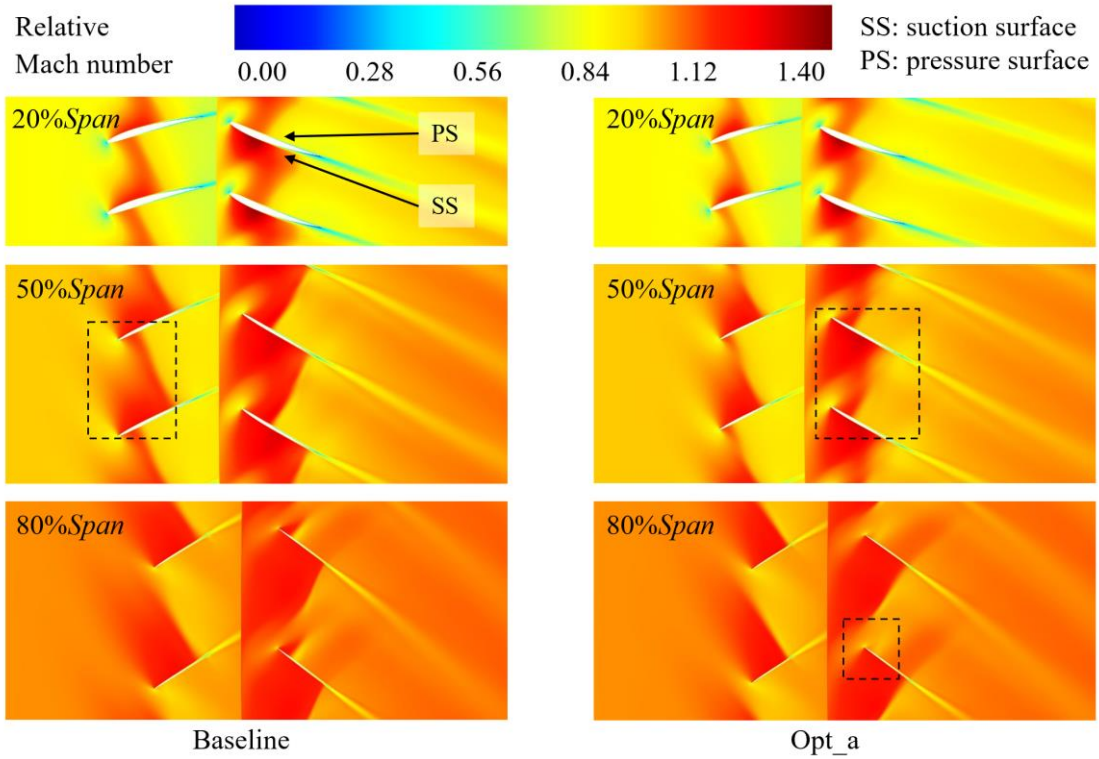

Fig. 22 Comparison of the relative Mach number distribution at different radial positions

increase in the torque share was accompanied by a slight increase in the propulsion efficiency, indicating better flow at the tip of *Opt_a*.

A comparison of the distribution of the relative Mach number before and after SBO is shown in Fig. 22. The reduced load illustrated in Fig. 21 and the decreased chord length of the FR at each blade height position caused the area of the high Mach number zone at the suction surface to be significantly reduced. For the rear rotor, at 50% height, the interaction between the blades was weakened. The increased angle of incidence weakened the shock at the pressure surface. A decrease in the camber angle weakened the shock at the suction surface. At the 80% height position, the high Mach number region at the leading edge of the pressure surface was eliminated and the shock at the pressure surface was reduced. This change was caused by an increase in the angle of incidence at 80% of the blade height. The shock at the blade channel was significantly reduced, which improved the flow conditions. This also explains the increase in the torque sharing at the top of the blade.

Figure 23 shows the static pressure coefficient distribution of the cross-section before and after optimization. The static pressure coefficient is defined as follows:

$$C_p = \frac{p - p_\infty}{\frac{1}{2}\rho_\infty v_\infty^2} \tag{16}$$

p is the static pressure. For the FR, there is a significant difference in the pressure coefficients before and after optimization owing to the significant change in the chord

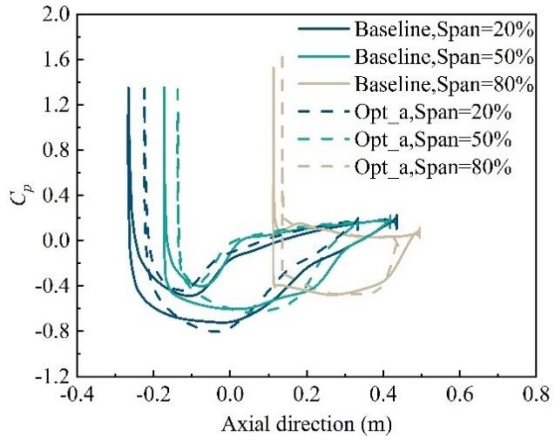

(a) Static pressure coefficients distribution of FR

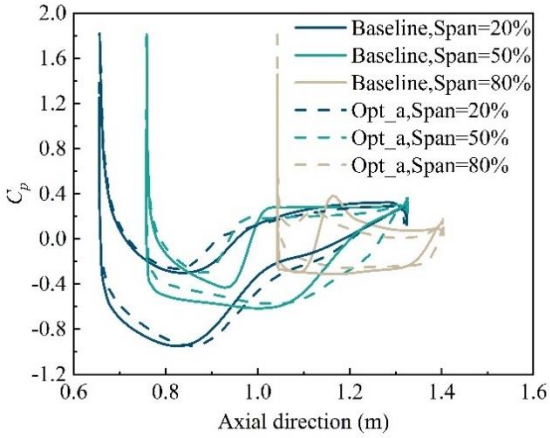

(b) Static pressure coefficients distribution of RR

Fig. 23 Comparison of the static pressure coefficients distribution on the blade surface

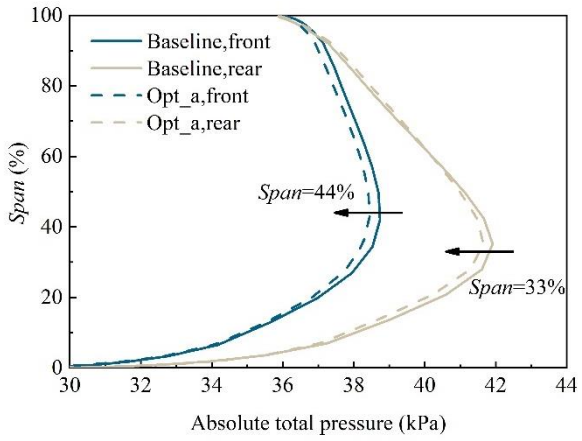

Fig. 24 Comparison of the absolute total pressure at rotors' outlet

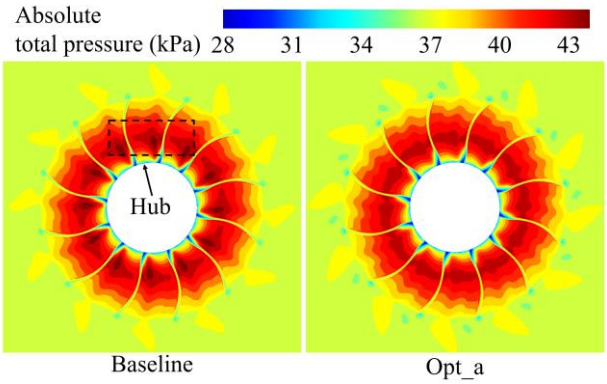

Fig. 25 Comparison of the total pressure at the CROR's outlet

length. Because the camber angle of the FR was almost unchanged and the stagger angle was only slightly reduced, there was no significant change in the pressure difference between the suction and pressure surfaces at 50% and 80% of the blade height. However, a reduction in chord length led to a reduction in the loading of the blade surface.

For the RR, the pressure coefficient distribution on the blade surface changed significantly owing to the significant changes in both the camber and stagger angles. The position with the lowest static pressure on the suction surface of the optimized rotor is moved backward, and the point of static pressure increase on the pressure surface is moved forward. In particular, at 80% of the blade height, the pressure distribution was greatly improved at the leading-edge position. The distribution of the static pressure coefficient at 50% of the blade height also indicated that the loading in the middle of the blade increased significantly.

Figure 24 shows a comparison of the absolute total pressure at the rotor outlet between the baseline and *Opt_a*. The baseline has a significant area of high total pressure at the middle of the blade. The optimization reduced the peak total pressure, resulting in a more uniform distribution of the total pressure at the blade outlet in the radial direction. The *Opt_a* shows an overall reduction in the total pressure at the front rotor outlet, especially at a blade height of 44% compared with the baseline. However, because of the increased torque in the RR, an overall reduction in the total pressure at the rear outlet does not occur. Only the peak total pressure at 33% of the blade height at the rear rotor outlet was reduced.

Figure 25 shows the total pressure distribution at the outlet of the CROR. At the outlet in the middle position, compared to the baseline, the optimized result had a more uniform total pressure distribution eliminating the local high total pressure region in the middle of the blade channel. The optimization resulted in a more circumferentially uniform distribution of total pressure at the outlet position.

6. CONCLUSION

This paper presents a surrogate-based optimization of the aerodynamic performance of a CROR using an infilling criterion. An infilling criterion is proposed based on the features of the rotor interactions. The SBO algorithm with infilling criterion and detailed implementation steps are presented.

During the SBO of the CROR, the characteristics of the constructed surrogate model are related to the features of the interaction between the two rows of rotors. Therefore, the features of the interactions were analyzed. The thrust of the front and rear rotors interacted with each other, and when one of them experienced a change in thrust owing to geometric changes, the thrust of the other changed significantly. However, this obvious interaction relationship does not exist in terms of the propulsion efficiency. When the FR deviates from ideal operating conditions, causing a decrease in the propulsion efficiency of the FR, the decrease in the rear rotor's propulsion efficiency is limited. These characteristics are also observed in the rear rotor. Therefore, it can be considered that the thrust of the rotors significantly affects each other; however, the propulsion efficiency depends more on their parameters. Additionally, when an efficient configuration is obtained, a wide range of thrust adjustments can be made by adjusting the geometric parameters without significantly reducing the propulsion efficiency. These two features result in an infilling criterion that applies to the optimization of the open rotor surrogate model. After obtaining the initial samples by numerical simulation, the efficient front and rear rotors of the initial samples were selected and combined to form new samples with high propulsion efficiency, thereby infilling points near the Pareto front.

Using this infilling criterion, an efficient surrogate-based optimization algorithm was developed. This algorithm was adopted to improve the rotors' propulsion efficiency while still achieving the target thrust coefficient. For the six optimization parameters, 20 initial sample points were used, and then 11 samples were infilled. The surrogate-based optimization was completed in five iterations. Overall sample points of seven times the optimized parameters were used to achieve the aerodynamic optimization of the CROR, which is less than that in existing studies. The results showed that the

infilling criterion caused the infilled samples to move toward the Pareto front, validating this algorithm. The optimization increased the torque share of the RR and changed the flow state at different radial positions, resulting in a more uniform total pressure distribution at the outlet, both circumferentially and radially. The optimization results showed an improved propulsion efficiency while meeting the thrust target.

ACKNOWLEDGEMENTS

The authors would like to acknowledge the financial support from the National Natural Science Foundation of China (No. 52076180), the Science Center for Gas Turbine Project (P2022-B-I-002-001, P2022-B-Ⅱ-010-001), the National Science and Technology Major Project (J2019-Ⅱ-0015-0036), the Funds for Distinguished Young Scholars of Shaanxi Province (2021JC-10), and the Fundamental Research Funds for the Central Universities

CONFLICT OF INTEREST

The authors declare that they have no conflict of interest.

AUTHORS CONTRIBUTION

Conceptualization, **Q. Wang**; Methodology, **Q. Wang**; Validation, **Q. Wang**; Formal analysis, **Q. Wang** and **L. Zhou**; Resources, **Q. Wang** and **L. Zhou**; Data curation, **Q. Wang**; Writing—original draft, **Q. Wang**; Writing—review and editing, **Q. Wang**, **L. Zhou** and **Z. Wang**; Visualization, **Q. Wang** and **L. Zhou**; Supervision, **L. Zhou** and **Z. Wang**; Project administration, **Z. Wang.** All authors have read and agreed to the published version of the manuscript.

REFERENCES

Adjei, R. A., Fan, C., Wang, W., & Liu, Y. (2021). Multidisciplinary design optimization for performance improvement of an axial flow fan using free-form deformation. *Journal of Turbomachinery*, *143*(1), 011003. https://doi.org/10.1115/1.4048793

Bellocq, P., Sethi, V., Capodanno, S., Patin, A., & Rodriguez Lucas, F. (2014). *Advanced 0-D performance modelling of counter rotating propellers for multi-disciplinary preliminary design assessments of open rotors.* ASME Paper No. GT2014-27141. https://doi.org/10.1115/GT2014-27141

Bellocq, P., Garmendia, I., & Sethi, V. (2015). *Preliminary design assessments of pusher geared counter-rotating open rotors: Part II—Impact of low pressure system design on mission fuel burn, certification noise and emissions.* ASME Paper No. GT2015-43816. https://doi.org/10.1115/GT2015-43812

Baert, L., Chérière, E., Sainvitu, C., Lepot, I., Nouvellon, A., & Leonardon, V. (2020). Aerodynamic optimization of the low-pressure turbine module: Exploiting surrogate models in a high-dimensional design space. *Journal of Turbomachinery*, *142*(3), 031005. https://doi.org/10.1115/1.4046232

Booker, A. J., Dennis, J. E., Frank, P. D., Serafini, D. B., Torczon, V., & Trosset, M. W. (1999). A rigorous framework for optimization of expensive functions by surrogates. *Structural Optimization*, *17*(1), 1-13. https://doi.org/10.1007/BF01197708

Boulkeraa, T., Ghenaiet, A., & Benini, E. (2022). Optimum operating parameters and blade setting of a high-speed propeller. *Journal of Aircraft*, *59*(2), 484-501. https://doi.org/10.2514/1.C035861

Cetin, M., Uecer, A. S., Hirsch, C., & Serovy, G. K. (1987). *Application of modified loss and deviation correlations to transonic axial compressors*. Neuilly-Sur-Seine, France: Advisory Group for Aerospace Research and Development.

Dubosc, M., Tantot, N., Beaumier, P., & Delattre, G. (2014, June 16-20). *A method for predicting contra rotating propellers off-design performance.* Proceedings of ASME Turbo Expo 2014: Turbine Technical Conference and Exposition, Düsseldorf, Germany. https://doi.org/10.1115/GT2014-25057

Forrester, A. I., & Keane, A. J. (2009). Recent advances in surrogate-based optimization. *Progress in Aerospace Sciences*, *45*(1-3), 50-79. https://doi.org/10.1016/j.paerosci.2008.11.001

Fang, K. T., Lin, D. K., Winker, P., & Zhang, Y. (2000). Uniform design: theory and application. *Technometrics*, *42*(3), 237-248. https://doi.org/10.1080/00401706.2000.10486045

GE36 Design and Systems Engineering (1987). *Systems engineering. Full-scale technology demonstration of a modern counter rotating unducted fan engine concept-design report*. NASA-CR-180867. https://ntrs.nasa.gov/citations/19900000732

Guérin, S., Schnell, R., & Becker, R. G. (2014). Performance prediction and progress towards multi-disciplinary design of contra-rotating open rotors. *The Aeronautical Journal*, *118* (1208), 1159-1179. https://doi.org/10.1017/S0001924000009830

Giunta, A., Wojtkiewicz, S., & Eldred, M. (2003, January 6-9). *Overview of modern design of experiments methods for computational simulations*. 41st Aerospace Sciences Meeting and Exhibit, Reno, NV. https://doi.org/10.2514/6.2003-649

Hoff, G. E., et al. (1990). *Experimental performance and acoustic investigation of modern, counterrotating blade concepts*. NASA-CR-185158, Washington, D. C.: NASA, 1990. https://ntrs.nasa.gov/citations/19900014077

Han, Z. H., Chen, J., Zhang, K. S., Xu, Z. M., Zhu, Z., & Song, W. P. (2018). Aerodynamic shape optimization of natural-laminar-flow wing using surrogate-based approach. *AIAA Journal*, *56*(7), 2579-2593. https://doi.org/10.2514/1.J056661

Jones, D. R., Schonlau, M., & Welch, W. J. (1998). Efficient global optimization of expensive black-box functions. *Journal of Global Optimization*, *13*(4), 455-492. https://doi.org/10.1023/A:1008306431147

Jones, D. R. (2001). A taxonomy of global optimization methods based on response surfaces. *Journal of Global Optimization*, *21*, 345-383. https://doi.org/10.1023/A:1012771025575

Jaron, R., Moreau, A., Guérin, S., & Schnell, R. (2018). Optimization of trailing-edge serrations to reduce open-rotor tonal interaction noise. *Journal of Fluids Engineering*, *140*(2), 021201. https://doi.org/10.1115/1.4037981

Kwon, H., Choi, S., Kwon, J. H., & Lee, D. (2016). Surrogate-based robust optimization and design to unsteady low-noise open rotors. *Journal of Aircraft*, *53*(5), 1448-1467. https://doi.org/10.2514/1.C033109

Li, Z. D, Chen, X. X., Wu, T., & Dong, W. (2022). Flow characteristics and pitch regulation of high-efficiency swept-curved counter rotating propellers. *Journal of Aerospace Power*, *37*(8), 1703-1713. https://doi.org/10.13224/j.cnki.jasp.20210278

Liu, Y., Wang, S., Li, K., Sun, W., & Song, X. (2022). An adaptive two-stage Kriging-based infilling strategy for efficient multi-objective global optimization. *Journal of Mechanical Design*, *144*(11), 111706. https://doi.org/10.1115/1.4055122

Montero Villar, G., Lindblad, D., & Andersson, N. (2018, June 25-29). *Multi-objective optimization of a counter rotating open rotor using evolutionary algorithms*. 2018 Multidisciplinary Analysis and Optimization Conference, Atlanta, GA. https://doi.org/10.2514/6.2018-2929

Montero Villar, G., Lindblad, D., & Andersson, N. (2019, January 7-11). *Effect of airfoil parametrization on the optimization of counter rotating open rotors*. AIAA Scitech 2019 Forum, San Diego, CA. https://doi.org/10.2514/6.2019-0698

Numeca International (2009). *FINE/Turbo v8.7, user manual*. Brussels: Belgium.

Persico, G., Rodriguez-Fernandez, P., & Romei, A. (2019). High-fidelity shape optimization of non-conventional turbomachinery by surrogate evolutionary strategies. *Journal of Turbomachinery*, *141*(8), 081010. https://doi.org/10.1115/1.4043252

Roache, P. J. (1997). Quantification of uncertainty in computational fluid dynamics. *Annual Review of Fluid Mechanics*, *29*(1), 123-160. https://doi.org/10.1146/annurev.fluid.29.1.123

Samad, A., Kim, K. Y., Goel, T., Haftka, R. T., & Shyy, W. (2008). Multiple surrogate modeling for axial compressor blade shape optimization. *Journal of Propulsion and Power*, *24*(2), 301-310. https://doi.org/10.2514/1.28999

Schnell, R., Yin, J., Voss, C., & Nicke, E. (2012). Assessment and optimization of the aerodynamic and acoustic characteristics of a counter rotating open rotor. *Journal of Turbomachinery*, *134*(6), 061016. https://doi.org/10.1115/1.4006285

Sasena, M. J., Papalambros, P., & Goovaerts, P. (2002). Exploration of metamodeling sampling criteria for constrained global optimization. *Engineering Optimization*, *34*(3), 263-278. https://doi.org/10.1080/03052150211751

Sohoni, N. G., Hall, C. A., & Parry, A. B. (2019). The influence of an upstream pylon on open rotor aerodynamics at angle of attack. *Journal of Turbomachinery*, *141*(2), 021006. https://doi.org/10.1115/1.4041082

Slaboch, P. E., Stephens, D. B., Van Zante, D. E., & Wernet, M. P. (2017). Effect of aft rotor on the inter-rotor flow of an open rotor propulsion system. *Journal of Engineering for Gas Turbines and Power*, *139*(4), 041202 https://doi.org/10.1115/1.4034356

Tang, Q., Wu, H., & Lou, H. (2022). Multi-objective optimization of aerodynamic performance for a small single-stage turbine. *Journal of Applied Fluid Mechanics*, *15*(5), 1451-1463. https://doi.org/10.47176/JAFM.15.05.33561

Viana, F. A., Haftka, R. T., & Watson, L. T. (2013). Efficient global optimization algorithm assisted by multiple surrogate techniques. *Journal of Global Optimization*, *56*(2), 669-689. https://doi.org/10.1007/s10898-012-9892-5

Yu, P. X., Peng, J. H., Bai, J. Q., Han, X., & Song, X. (2020). Aeroacoustic and aerodynamic optimization of propeller blades. *Chinese Journal of Aeronautics*, *33*(3), 826-839. https://doi.org/10.1016/j.cja.2019.11.005

Zachariadis, A., & Hall, C. A. (2011). Application of a Navier-Stokes solver to the study of open rotor aerodynamics. *Journal of Turbomachinery*, *133*(3), 031025. https://doi.org/10.1115/1.4001246